

Investigation on Elasticity-Based Tissue Characterization of Arterial Wall

Hideyuki Hasegawa^{1,2} and Hiroshi Kanai^{2,1}

1 Graduate School of Biomedical Engineering,

2 Graduate School of Engineering

E-mail: hasegawa@ecei.tohoku.ac.jp, hkanai@ecei.tohoku.ac.jp



Abstract

Pathological changes in arterial walls significantly influence their mechanical properties. We have developed a correlation-based method, the *phased tracking method*, for measurement of the regional elasticity of the arterial wall. Using this method, elasticity distributions of lipids, blood clots, fibrous tissue, and calcified tissue were measured by *in vitro* experiments of excised arteries (mean \pm SD: lipid 89 ± 47 kPa, blood clot 131 ± 56 kPa, fibrous tissue 1022 ± 1040 kPa, calcified tissue 2267 ± 1228 kPa). It was found that arterial tissues can be classified into soft tissues (lipids and blood clots) and hard tissues (fibrous tissue and calcified tissue) on the basis of their elasticity. However, there are large overlaps between elasticity distributions of lipids and blood clots and those of fibrous tissue and calcified tissue. Thus, it was difficult to differentiate lipids from blood clots and fibrous tissue from calcified tissue by setting a threshold for a single elasticity value. Therefore, we previously proposed a tissue classification method using the elasticity distribution in each small region. In this method, the elasticity distribution of each small region of interest (ROI) (not a single pixel) in an elasticity image is used to classify lipids, blood clots, fibrous tissue, and calcified tissue by calculating the likelihood function for each tissue. In the present study, the optimum size of the ROI and threshold T_o for the likelihood function were investigated to improve the tissue classification. The ratio of correctly classified pixels to the total number of classified pixels was 29.8% when the size of a small region was $75 \mu\text{m} \times 300 \mu\text{m}$ (a single pixel). The ratio of correctly classified pixels became 54.2% when the size of a small region was $1,500 \mu\text{m} \times 1,500 \mu\text{m}$ (100 pixels). In this classification, a region with an extremely low likelihood with respect to all tissue components was defined as an unclassified region by setting threshold T_o for the likelihood function. The optimal threshold was determined from the standard deviation in the measurements of radial strains evaluated by basic experiments using a phantom. The tissue classification of the arterial wall was improved using the elasticity distribution of a small region whose size was larger than the spatial resolution ($800 \mu\text{m} \times 600 \mu\text{m}$) of ultrasound.

1. Introduction

Noninvasive measurement of mechanical properties of the arterial wall, such as elasticity, is useful for diagnosing atherosclerosis because there are significant differences between the elastic moduli of normal arterial walls and those affected by atherosclerosis [1][2][3]. In particular, mechanical properties of plaque are important because the rupture of plaque may cause acute myocardial infarction and cerebral infarction [4][5][6]. Magnetic resonance imaging (MRI) and intravascular ultrasound (IVUS) are promising technologies for directly imaging plaque morphology [7][8]. On the other hand, the dynamic change of artery diameter due to the pulsation of the heart can be measured noninvasively by the previous method with ultrasound [9][10][11][12][13]. Some parameters related to artery-wall elasticity can be obtained by the measured change in diameter of the artery [14][15][16]. However, in the derivation of these parameters, the artery is assumed to be a cylindrical shell with a uniform wall thickness and, thus, the elasticity of atherosclerotic plaque cannot be evaluated.

For measurement of the mechanical properties of the arterial wall, including the case with atherosclerotic plaque, we previously developed a method, namely, the *phased tracking method*, for measuring small vibrations in the heart wall or arterial wall with transcutaneous ultrasound [17][18]. For some years, we have been measuring the displacement and small change in thickness of the arterial wall caused by the heartbeat using this method [19][20][21][22]. In our *phased tracking method*, a set of two points is assigned along an ultrasonic beam, and the change in thickness of the layer between these two points is estimated. Furthermore, by sliding the position of the layer along the ultrasonic beam by intervals of the sampled points, the spatial distribution of changes in thickness along the ultrasonic beam can be obtained.

In the estimation of the change in thickness using a correlation estimator, the thickness of an assigned layer is larger than the interval of the sampled points, and the layer is slid by the intervals of the sampled points. Therefore, several layers with respective correlation estimators overlap at each depth. Therefore, correlation estimators of layers, which overlap at a certain depth, are compounded to obtain the change in thickness at that depth [23]. Although the angle of the ultrasonic beam was not changed in the present study, the concept of spatial compounding has been applied in previous

studies to magnitudes of echoes, which are obtained by scanning each point in the ROI with ultrasonic beams having different beam angles, to improve B-mode images [24].

Elasticity images of the human carotid artery have been obtained by the measured displacement distribution, and the potential for transcutaneous tissue characterization has been shown by classifying the elasticity images using the elasticity reference data obtained by *in vitro* experiments [22][25][26].

We have already measured the elasticity distributions for lipids, blood clots, fibrous tissue (mixture of the smooth muscle and collagen), and calcified tissue. In these previous studies, it was found that arterial tissues can be classified into soft tissues (lipids, blood clots) and hard tissues (fibrous tissue, calcified tissue) on the basis of their elasticity. However, it was difficult to differentiate lipids from blood clots and fibrous tissue from calcified tissue. Therefore, we proposed a tissue classification method using the elasticity distribution in a small region [27]. In this method, the elasticity distribution of each small ROI (not a single pixel) in an elasticity image was used in classification of lipids, blood clots, fibrous tissue, and calcified tissue. Precision of tissue classification was improved using the elasticity distribution in each small region.

However, the accuracy of this method in relation to the size of an ROI has not yet been thoroughly investigated, and the method has not been applied to the differentiation of fibrous tissue from calcified tissue. In the present study, to determine the optimum size of an ROI, the accuracy of tissue classification (including calcified tissue) was quantitatively investigated in relation to the size of the ROI by evaluating the ratio of the number of correctly classified pixels to the total number of classified pixels. In addition, in the proposed classification method, the likelihood function of each small ROI is obtained for each tissue component (lipids, blood clots, fibrous tissue, and calcified tissue), and the region is classified into a tissue component that shows the maximum likelihood. However, an ROI is classified into one of the four tissue components even when the maximum likelihood is low. In the present study, such a region is defined as an unclassified region by setting a threshold for the likelihood. From these investigations, tissue classification was much improved in comparison with that in the previous study [28][29].

2. Materials and Methods

2.1. Experimental setup and specimens

Figure 1 shows a schematic diagram of the measurement system. The change in pressure inside the artery was realized by circulating a fluid using a flow pump. The fluid inside the artery and that circulating in the flow pump were separated by a rubber membrane to prevent the flow pump from being contaminated, and only the change in internal pressure propagated to the inside of the artery. The change in internal pressure

was measured by a pressure transducer (Model 110-4, Camino, San Diego, CA, USA).

In ultrasonic measurement, excised arteries were measured with a conventional 7.5 MHz linear-type ultrasonic probe (SSH-140A, Toshiba, Japan). The quadrature demodulated signals of RF echoes were acquired at 10 MHz at a frame rate of 200 Hz. In this study, the elasticity of the arterial wall is defined as the tissue strain calibrated by the average stress of the entire wall thickness, namely, circumferential elastic modulus E_{θ}^h [25]. The strain distribution is obtained by applying the *phased tracking method* to the measured demodulated signals [21][23].

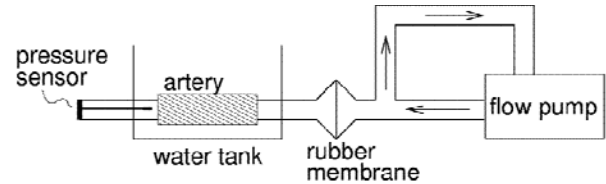


Fig. 1. Schematic diagram of the measurement system.

In this study, eight iliac and ten femoral arteries which had been surgically excised from eighteen patients with arteriosclerosis obliterans were measured *in vitro*. These arteries had been excised at the time of bypass grafting surgery. During the ultrasonic measurement, a needle was attached to the external surface of the artery for identification of the measured section so that a pathological image of the same section could be obtained after the ultrasonic measurement. This study was approved by the Ethics Committee on Clinical Investigation, Graduate School of Engineering, Tohoku University, and was performed in accordance with the policy of the Declaration of Helsinki; all subjects gave informed consent.

2.2. Tissue classification using the likelihood function

In this study, each pixel in an elasticity image is classified into one of 5 categories of lipids, blood clots, fibrous tissue, calcified tissue, and unknown using the likelihood function $\{L_i\}$ ($i = 1$: lipid, 2: blood clot, 3: fibrous tissue, 4: calcified tissue) of the elasticity distribution in the small region around the pixel. To obtain the likelihood function $\{L_i\}$, the elasticity distribution of the i -th tissue is translated into the normal distribution to describe the probability distribution by the mean and the standard deviation as described below [27].

From *in vitro* experiments, the elasticity distribution of each tissue i is obtained as illustrated in Fig. 2(a). The elasticity distribution of the i -th tissue consists of J_i data points with the respective elastic moduli. Using all data of J_i points (J_1 : 228, J_2 : 179, J_3 : 19,121, J_4 : 1,101) with the respective elastic moduli, the ascending sequence is constructed for tissue i as shown in Fig. 2(b). In this sequence, the j -th datum ($j = 1, 2, \dots, J_i$) has the corresponding elastic modulus E_j ($E_j \leq E_{j+1}$),

where j is termed the elasticity number. The probability distribution of each tissue was obtained by allocating all the data of J_i points of each tissue i to boxes of the normal distribution. The box numbers, $\{B_i\}$, of the normal distribution are determined so that the number of data in the box at each end is only one. As shown in Fig. 2(c), the number of data, $D_{i,h}$ ($h = 1, 2, \dots, B_i$), included in box B_i is determined so as to follow the profile of the normal distribution. Thus, the $(J_i/2)$ -th datum is included in the box with the highest probability. By allocating all the data of J_i points of each tissue to boxes of the corresponding normal distribution, the mean elasticity $\bar{E}_{i,h}$ of the data included in each box is obtained.

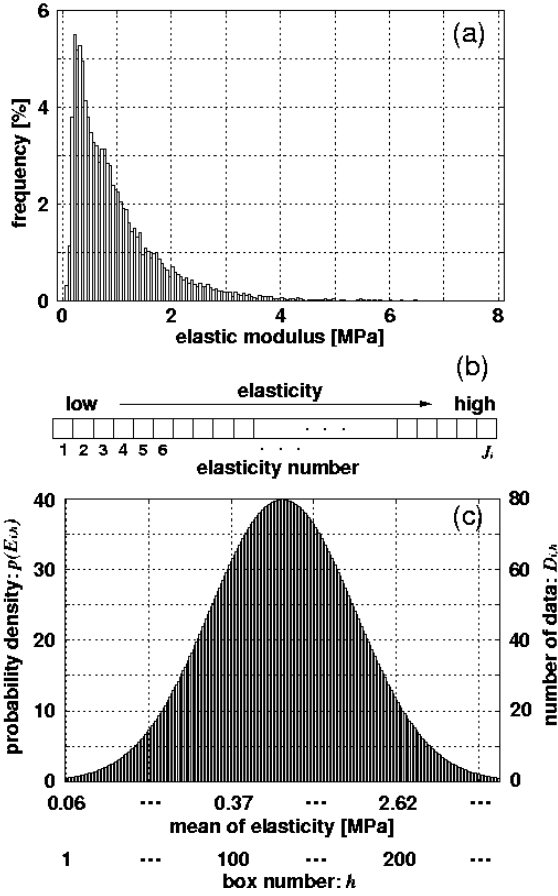


Fig. 2. (a) Original elasticity distribution of the tissue. (b) Ascending sequence of elastic modulus in an elasticity distribution. (c) Normal distribution whose number of boxes depends on the number of data points of (a).

As shown in Fig. 3, an ROI was assigned to an elasticity image which was obtained by ultrasonic measurement. The likelihood function $L_i(m,n)$ is defined as a joint probability that all the elasticity values in ROI $R_{m,n}$ (center of ROI: n -th sampled point along m -th beam) simultaneously belong in the i -th category as follows:

$$L_i(m,n) = \left(\prod_{(k,l) \in R_{m,n}} p_i(E_{k,l}) \right)^{1/N_0} \quad (i = 1, 2, 3, 4) \quad (2.1)$$

where $p_i(E_{k,l})$ is the probability density which shows the probability that elasticity value $E_{k,l}$ in the k -th row and l -th column in the ROI belongs to the i -th tissue category, and N_0 denotes the number of pixels in an ROI $R_{m,n}$. The multiplier $1/N_0$ shows the geometric mean for compensation of the effect of the size of an ROI. The pixel at the center of an ROI is classified into the class which has the maximum likelihood.

In this classification, there may be a region which has an extremely small value for the maximum likelihood. Such regions are classified into the unclassified region by setting threshold T_o to the maximum likelihood. Thus, the category $C(R_{m,n})$, to which an ROI $R_{m,n}$ belongs, is expressed as follows:

$$C(R_{m,n}) = \begin{cases} \arg \max_{1 \leq i \leq 4} L_i(m,n) \\ \text{(if } \max_{1 \leq i \leq 4} L_i(m,n) \geq T_o \text{)} \\ \text{unknown} \quad \text{(otherwise)} \end{cases} \quad (2.2)$$

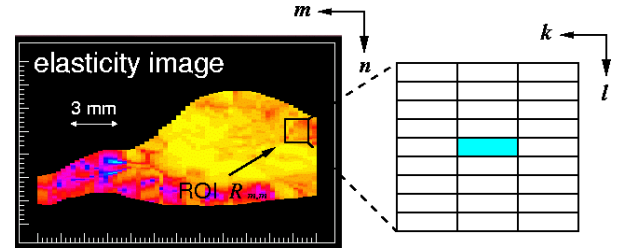


Fig. 3. Illustration of region of interest (ROI).

Figure 4 shows examples of tissue classification images which were manually estimated by referring to the pathological images of iliac arteries (A) and (B). By comparing the pathology-based classification images shown in Fig. 4 with the tissue classification images obtained by the proposed method, the recognition rate $R_r(S_{ROI})$ for all tissues in the arterial wall was defined by the ratio of the number of correctly classified pixels to the number N of all pixels in the image as follows:

$$R_r(S_{ROI}) = \frac{\sum_i N_i}{N} \times 100 [\%], \quad (2.3)$$

where N_i is the number of correctly classified pixels of tissue i and S_{ROI} is the size of an ROI. Recognition rate $R_r(S_{ROI})$ was used to determine the optimum size of an ROI.

3. In Vitro Experiments for Construction of “Elasticity Library”

Figure 5(a) shows a B-mode image of one of the femoral arteries. The strong echoes from outside the femoral arteries. The strong echoes from outside the posterior wall correspond to a needle. For the posterior wall, the images of the maximum change in thickness

during a cycle of the flow pump were measured as shown in Fig. 5(b).

Figure 6(a) shows the elasticity image of the femoral artery obtained from the maximum change in internal pressure and that in thickness obtained by the *phased tracking method* shown in Fig. 5(b). By referring to the pathological image of the same section shown in Fig. 6(b), fibrous tissue in the intima-media region was identified. The corresponding region, namely, the region surrounded by the green line in Fig. 6(a), was then assigned to the elasticity image. Figure 6(c) shows the elasticity distribution of fibrous tissues extracted from the region surrounded by the green line in Fig. 6(a). By applying the same procedure to the other arteries, the elasticity distribution of each tissue in the arterial wall was obtained.

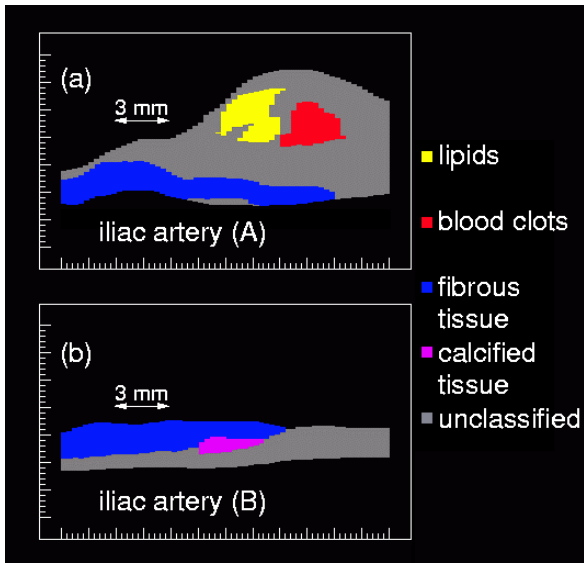


Fig. 4. Tissue classification images obtained by referring to pathological images. (a) Iliac artery (A). (b) Iliac artery (B).

Figure 7 shows the elasticity distribution of each tissue, that is, the frequency of the elasticity values which belong to the range defined by the position and width of each vertical bar. The width of a vertical bar was set at 50 kPa. Means and standard deviations are 89 ± 47 (lipids), 131 ± 56 (blood clots), $1,022 \pm 1,040$ (fibrous tissue), and $2,267 \pm 1,228$ kPa (calcified tissue). Although similarities were found in the elasticity distributions of lipids and blood clots and in those of fibrous and calcified tissues, differences in the elasticity distributions of these tissues were found.

4. Determination of the Optimal Size of a Region of Interest

Figure 8 shows the probability density of each tissue obtained by the axis transformation of the elasticity distribution. As shown in these figures, the horizontal axis showing the elastic modulus is nonlinear. Using

these databases, each pixel in an elasticity image was classified as a certain tissue component.

Figures 9(c) and 9(d) show the tissue classification results obtained by the proposed method for the iliac artery (A). The regions classified as lipids, blood clots, fibrous tissue, and calcified tissue were stained yellow, red, blue, and purple, respectively. Figure 9(c) graphically shows the tissue classification image obtained with an ROI size of 1×1 pixel. Although arterial tissues were roughly classified into soft tissues (lipids and blood clots) and hard tissues (fibrous tissue and calcified tissue), the classified tissue distributions are scattered, and the misclassified regions are outstanding. Alternatively, Fig. 9(d) shows the result of classification with an ROI size of $1,500 \mu\text{m}$ ($= 20$ pixels) in the radial direction and $1,500 \mu\text{m}$ ($= 5$ pixels) in the longitudinal direction. Moreover, the region with low likelihood for all tissue components is colored gray. The threshold T_o for the maximum of the likelihood functions $\{L_i\}$ was set at 0.21. As shown in Fig. 9(d), the region with the maximum likelihood which is higher than threshold T_o is accurately classified as the corresponding tissue identified by referring to the pathological image.

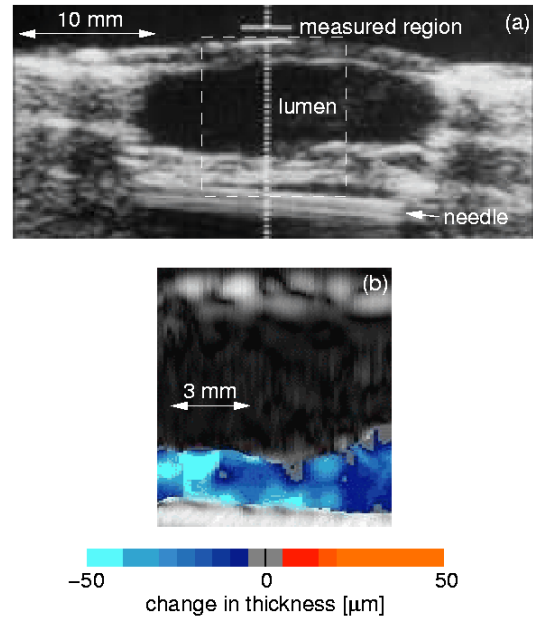


Fig. 5. (a) B-mode image of a femoral artery. (b) Image of the maximum change in thickness during the cardiac cycle.

For another specimen (iliac artery (B)), calcified tissue in the fibrous tissue was identified as shown in Fig. 10(e). As in Fig. 8, tissue classification was improved using the elasticity distribution of each ROI (not a single pixel). In the case of Fig. 10, there was no region with low likelihood for any of the tissue components.

Figure 11 shows the relationship between the size S_{ROI} of an ROI and the recognition rate $R_r(S_{\text{ROI}})$. The ROI size S_{ROI} was changed with its shape being kept

square. In Fig. 11, the horizontal axis shows the width $W = \sqrt{S_{\text{ROI}}}$ of an ROI in the longitudinal direction.

An ROI consists of a single pixel when the width, W , in Fig. 11 is 0.3 mm. Only in this specific case, is an ROI not square ($75 \mu\text{m} \times 300 \mu\text{m}$). Figure 11(b) shows the relationship between width $W = \sqrt{S_{\text{ROI}}}$ of an ROI in the longitudinal direction and the recognition rate $R_r(S_{\text{ROI}})$ in arteries which are composed of a single type of tissue, such as fibrous tissue. In such case, the recognition rate $R_r(S_{\text{ROI}})$ is monotonically improved by increasing the size of an ROI because an elasticity image is uniformly classified as the corresponding tissue using a large ROI, which results from the worsening spatial resolution in tissue classification. Figure 11(a) shows the relationship between width W of an ROI and the recognition rate $R_r(S_{\text{ROI}})$ in arteries composed of different types of tissues. For this case, tissue classification using some pixels in an ROI is superior to that using a single pixel. However, the improvement of tissue classification by the enlargement of an ROI is limited because the classification using a large ROI provides a uniform tissue classification image whereas the arterial wall is composed of different kinds of tissues. Therefore, there should be an optimum size of an ROI. As shown in Fig. 11(a), the recognition rates became maximum in most arteries when the size of an ROI was $1,500 \mu\text{m} \times 1,500 \mu\text{m}$.

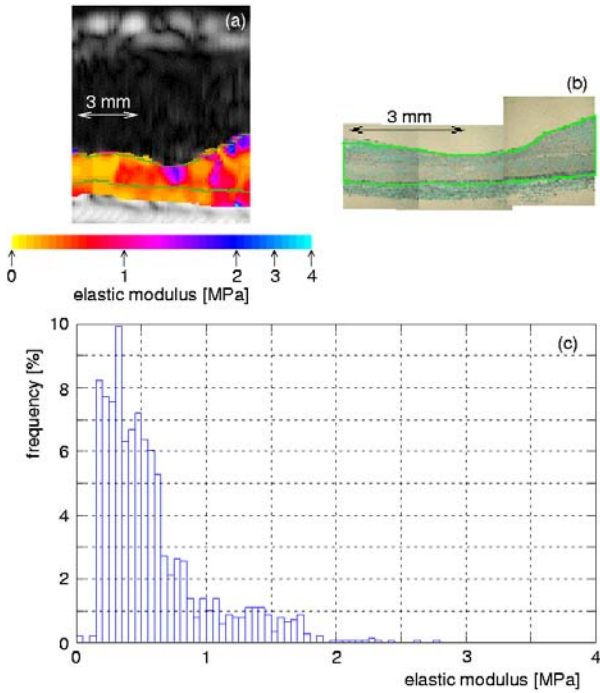


Fig.6. (a) Elasticity image of the arterial wall. (b) Pathological image of the corresponding section. (c) Elasticity distribution in the region between the two green lines in (a).

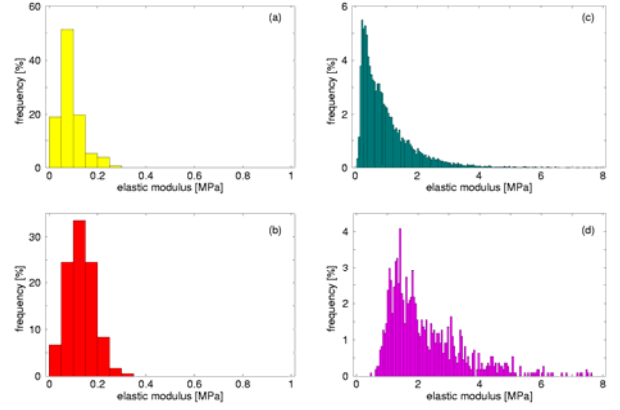


Fig. 7. Elasticity distribution of each tissue. (a) Lipids ($N = 288$). (b) Blood clots ($N = 178$). (c) Fibrous tissue ($N = 19,120$). (d) Calcified tissue ($N = 1,101$).

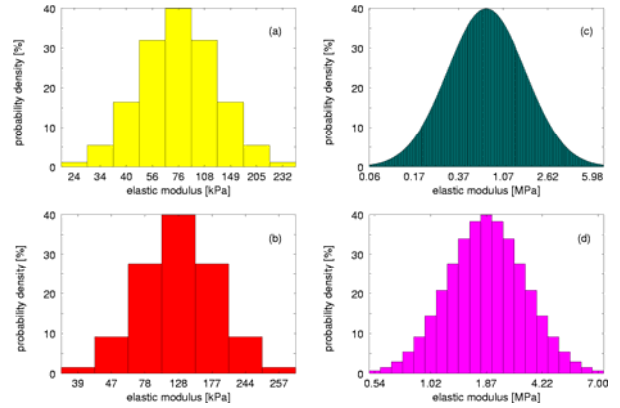


Fig. 8. Probability density for each tissue. (a) Lipids. (b) Blood clots. (c) Fibrous tissue. (d) Calcified tissue.

5. Determination of the Optimal Threshold

5.1 Basic experiments using a phantom for evaluation of variance in measurement of radial strain

A homogeneous cylindrical phantom (internal radius: $r_i = 4 \text{ mm}$, external radius: $r_o = 5 \text{ mm}$, elastic modulus: $E = 750 \text{ kPa}$) made from silicone rubber containing 5% carbon powder by weight was measured with a 7.5 MHz linear ultrasonic probe. The scan plane was parallel to the longitudinal direction of the phantom, and the directions of all ultrasonic beams coincided with the radial direction of the phantom. The change in internal pressure, which was applied using a flow pump, was measured by a pressure sensor. The sampling frequency of the quadrature demodulated signal and the frame rate were 10 MHz and 200 Hz, respectively. The theoretical value of radial strain $\Delta\epsilon_r(r)$ at each radial position r is obtained by [30]

$$\Delta\epsilon_r(r) = -\frac{3}{2} \frac{r_i^2 r_o^2}{r_o^2 - r_i^2} \frac{\Delta p}{E r^2}, \quad (5.1)$$

where Δp is the pressure increment. The radial strain measured by the *phased tracking method* was compared with the theoretical value $\Delta \varepsilon_r(r)$.

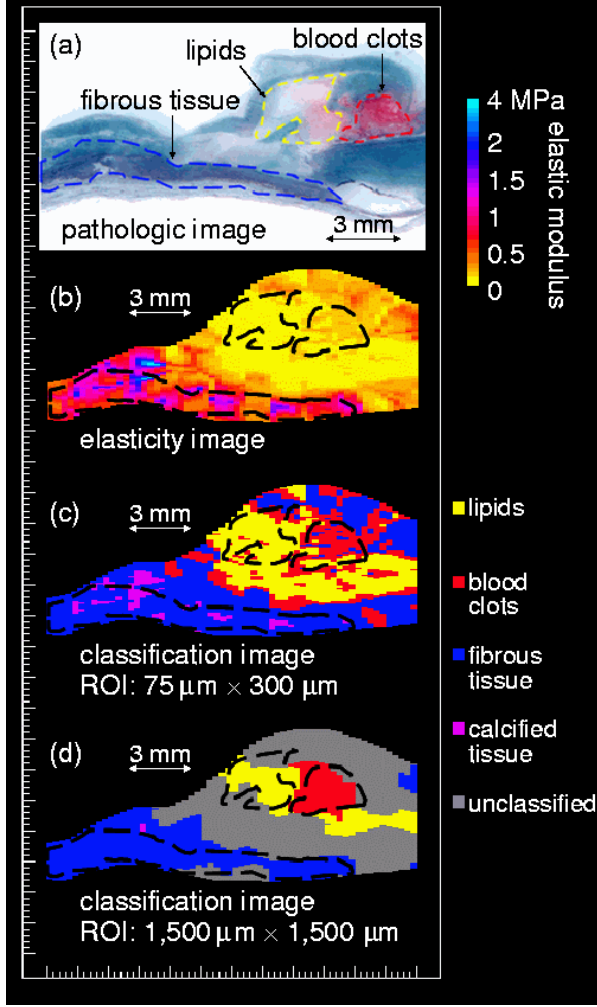


Fig. 9. For the iliac artery (A). (a) Pathological image of an arterial wall subjected to elastica-Masson staining. (b) Elasticity image. (c) Tissue classification image (ROI size: 1×1 pixel). (d) Tissue classification image (ROI size: 5×20 pixels).

Figures 12(a)-12(d) show the strain distribution along the radial direction of the phantom obtained by the *phased tracking method* for cases of pressure increments $\Delta p = 40, 50, 60,$ and 70 mmHg, respectively. Plots and vertical bars show means and standard deviations for 60 ultrasonic beams. The difference between the mean and the theoretical value is lower than the standard deviation, and mean value follows the theoretical profile.

Figure 13 shows the relationship between the mean μ_s and the standard deviation σ_s normalized by the mean value. The plots and the straight line show all the measured results in Fig. 12 and the regression line, respectively. A positive correlation was found between the mean μ_s and the normalized standard deviation σ_s , because the standard deviation was almost constant

over every pressure increment. The regression line was determined as follows:

$$\sigma_s = 7.1 \cdot \mu_s + 0.40. \quad (5.2)$$

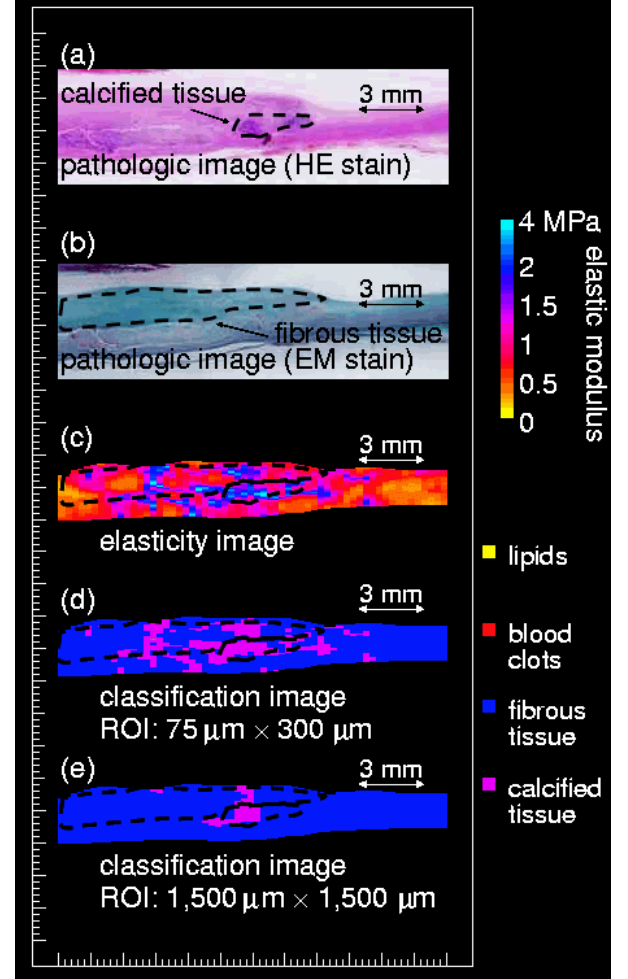


Fig. 10. For the iliac artery (B). (a) Pathological image of another arterial wall subjected to hematoxylin-eosin staining. (b) Pathological image of the arterial wall subjected to elastica-Masson staining. (c) Elasticity image. (d) Tissue classification image (ROI size: 1×1 pixel). (e) Tissue classification image (ROI size: 5×20 pixels).

The threshold $T_{o,i}(R_{m,n})$ for likelihood function $L_i(m, n)$ of tissue i of each ROI $R_{m,n}$ is determined using the experimental results with the phantom. Using eq. (5.2), the normalized standard deviation $\sigma_s(R_{m,n})$ in the measurement of the radial strain in $R_{m,n}$ was given approximately by:

$$\sigma_s(R_{m,n}) = 7.1 \cdot \bar{\mu}(R_{m,n}) + 0.40, \quad (5.3)$$

$$\bar{\mu}(R_{m,n}) = \frac{1}{N_0} \sum_{(k,l) \in R_{m,n}} \varepsilon_{\max}(k,l), \quad (5.4)$$

where $\varepsilon_{\max}(k, l)$ and $\bar{\mu}$ are the maximum radial strain during one cardiac cycle in the k -th row and l -th column

and the average of the maximum radial strain in $R_{m,n}$, respectively.

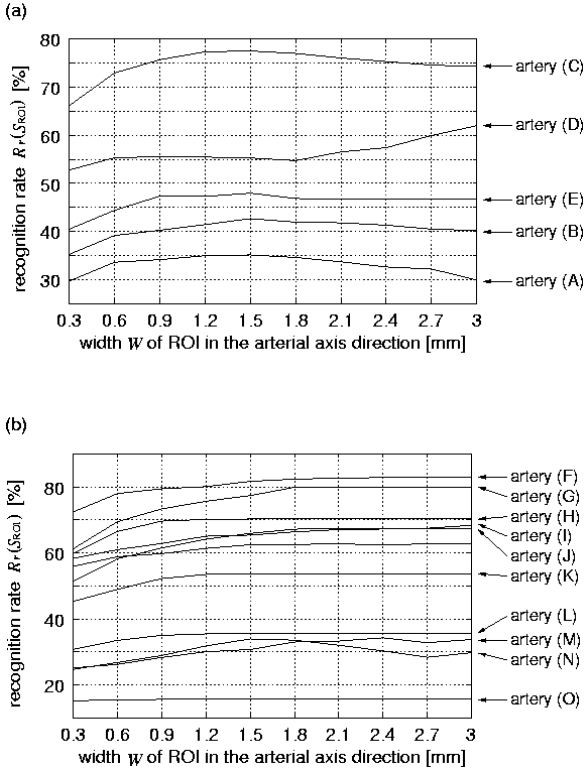


Fig. 11. Relationship between width W of an ROI in the longitudinal direction and the recognition rate $R_r(S_{ROI})$. (a) Arteries composed of several types of tissues. (b) Arteries composed of a single tissue. Each line shows the recognition rate $R_r(S_{ROI})$ of the corresponding artery.

Figure 14 shows an illustration for determining the threshold $T_{o,i}(R_{m,n})$ for the likelihood function $L_i(m, n)$ of tissue i . Let us consider the elasticity distribution in an ROI. Variance $\sigma_0^2(R_{m,n})$ of the measured elasticity $\hat{E}_{k,l}$ in the k -th row and l -th column in $R_{m,n}$ is expressed as follows:

$$\sigma_0^2(R_{m,n}) = E_{(k,l) \in R_{m,n}} [\hat{E}_{k,l}^2] - \left(\bar{\hat{E}}_{R_{m,n}} \right)^2, \quad (5.5)$$

where $E_{(k,l) \in R_{m,n}}[\cdot]$ shows the averaging for the data included in the ROI $R_{m,n}$, and $\bar{\hat{E}}_{R_{m,n}}$ is the average of the measured elasticity values $\{\hat{E}_{k,l}\}$ in $R_{m,n}$. By assuming that the true elasticity values $\{E_{k,l}\}$ are not constant in $R_{m,n}$ due to the elasticity inhomogeneity of tissue even when there is no measurement error, the measured elasticity $\{\hat{E}_{k,l}\}$ is described by the sum of true elasticity $\{E_{k,l}\}$ and the error $\{\Delta E_{k,l}\}$ (sum of random error $\{e_{k,l}\}$ and bias error $b_{R_{m,n}}$) as follows:

$$\hat{E}_{k,l} = E_{k,l} + \Delta E_{k,l}, \quad (k,l) \in R_{m,n}. \quad (5.6)$$

Thus, the mean $\bar{\hat{E}}_{R_{m,n}}$ of the measured elasticity values $\{\hat{E}_{k,l}\}$ is given by

$$\bar{\hat{E}}_{R_{m,n}} = \bar{E}_{R_{m,n}} + b_{R_{m,n}}, \quad (5.7)$$

where $\bar{E}_{R_{m,n}}$ and $b_{R_{m,n}}$ are the true mean elasticity in $R_{m,n}$ and the bias error $b_{R_{m,n}} = E_{(k,l) \in R_{m,n}}[\Delta E_{k,l}]$, respectively. By substituting eq. (5.7), eq. (5.5) is modified as follows:

$$\begin{aligned} \sigma_0^2(R_{m,n}) = & E_{(k,l) \in R_{m,n}} \left[\left(E_{k,l} - E_{(k,l) \in R_{m,n}}[E_{k,l}] \right)^2 \right] + E_{(k,l) \in R_{m,n}} \left[\left(e_{k,l} - \bar{e}_{R_{m,n}} \right)^2 \right] \\ & + 2 E_{(k,l) \in R_{m,n}} [E_{k,l} \cdot e_{k,l}] + 2b_{R_{m,n}} E_{(k,l) \in R_{m,n}} [e_{k,l}] \end{aligned} \quad (5.8)$$

where $\bar{e}_{R_{m,n}}$ is assumed to be zero because $\{e_{k,l}\}$ is random error. Variance $(\sigma_e(R_{m,n}))^2$ of the measurement error $\{e_{k,l}\}$ in $R_{m,n}$ is expressed by $(\sigma_e(R_{m,n}))^2 = (\sigma_s(R_{m,n}) \cdot \bar{\hat{E}}_{R_{m,n}})^2$, where $\sigma_s(R_{m,n})$ is determined by eq. (5.3). By defining the variance due to the elastic inhomogeneity of tissue in $R_{m,n}$ by $\sigma(R_{m,n})^2$ eq. (5.8) is expressed as follows:

$$\sigma_0^2(R_{m,n}) = (\sigma(R_{m,n}))^2 + \left(\sigma_s(R_{m,n}) \cdot \bar{\hat{E}}_{R_{m,n}} \right)^2 + 2 E_{(k,l) \in R_{m,n}} [E_{k,l} \cdot e_{k,l}] \quad (5.9)$$

where there is no correlation between the inhomogeneity of $E_{k,l}$ and $\{e_{k,l}\}$ in $R_{m,n}$. Therefore, variance $(\sigma(R_{m,n}))^2$ without error of eq. (5.9) is given by $\{\sigma_s(R_{m,n}) \bar{\hat{E}}_{R_{m,n}}\}^2$ subtracted from the variance σ_0^2 of the measured elasticity values $\{\hat{E}_{k,l}\}$ in $R_{m,n}$ as follows:

$$\sigma^2(R_{m,n}) = \sigma_0^2(R_{m,n}) - \left\{ \sigma_s(R_{m,n}) \cdot \bar{\hat{E}}_{R_{m,n}} \right\}^2. \quad (5.10)$$

Based on this relation, by setting the acceptance region [from $-\alpha\sigma_i(R_{m,n})$ to $\alpha\sigma_i(R_{m,n})$] of the probability density $N(\mu_i, \sigma_i^2(R_{m,n}))$ for each tissue i , the threshold $T_{o,i}(R_{m,n})$ for the likelihood function $L_i(m, n)$ of tissue i in $R_{m,n}$ was determined by the probability of the distribution $N(\mu_i, \sigma_{0,i}^2(R_{m,n}))$ with the error at the distance from mean μ_i as shown in Fig. 15. Therefore, the threshold $T_{o,i}(R_{m,n})$ for the likelihood function $L_i(m, n)$ of tissue i is given by

$$T_{o,i}(R_{m,n}) = \frac{1}{\sqrt{2\pi}\sigma_{0,i}} \exp \left[-\frac{\left(\left(\alpha \sqrt{\sigma_0^2(R_{m,n}) - \left\{ \sigma_s(R_{m,n}) \bar{\hat{E}}_{R_{m,n}} \right\}^2} \right)^2 \right)}{2\sigma_{0,i}^2} \right], \quad (5.11)$$

where $\sigma_{0,i}$ is the variance of measured elasticity distribution for tissue i .

Figures 16(c)-16(g) show the tissue classification images for an excised human iliac artery (A). The regions classified as lipids, blood clots, fibrous tissue, and calcified tissue are color-coded yellow, red, blue, and purple, respectively. Figure 16(c) shows the classification image obtained with an ROI size of 5×20 pixels ($1,500 \times 1,500 \mu\text{m}^2$) without thresholding. Although the pixels were roughly classified into the correct tissues, the pixels which have low likelihood $L_i(m, n)$ were also classified. Figures 16(d)-16(g) show the classification images obtained with thresholds $T_{o,i}(R_{m,n})$ determined at four different area ratios of $w = 99, 95, 90,$ and 85% , respectively. In Figs. 16(d)-16(g), a region whose likelihood is less than the threshold $T_{o,i}(R_{m,n})$ for all tissue components is colored gray. As shown in Figs. 16(d)-16(g), similarities among the classification images seem to be qualitatively high especially for those at an area ratio w less than or equal to 95% . It can be expected from the result shown in Fig. 17 that improvement in the recognition rate $R_r(w)$ by decreasing area ratio w slightly diminish at area ratio w less than 95% . For these results, the misclassification was reduced using the threshold $T_{o,i}(R_{m,n})$ determined from the area ratio of the acceptance region less than or equal to 95% .

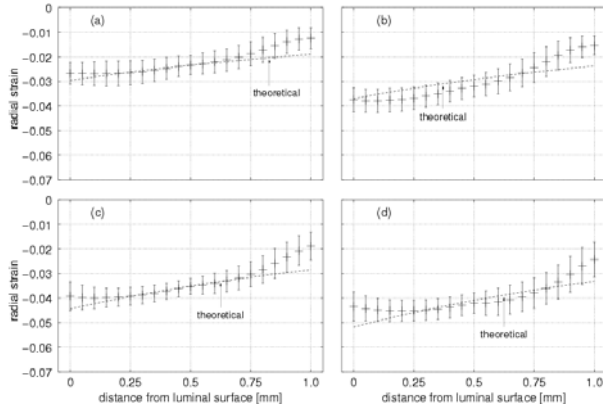


Fig. 12. Estimated strains of the phantom, plotted as a function of the distance from the lumen. (a) $\Delta p = 40$ mmHg. (b) $\Delta p = 50$ mmHg. (c) $\Delta p = 60$ mmHg. (d) $\Delta p = 70$ mmHg.

4. Conclusion

In this study, tissue classification based on the likelihood function with the configured appropriate ROI size (not a single pixel) and a lower limit of likelihood were investigated. Using the elasticity distribution in an ROI, the differentiation of lipids from blood clots and that of fibrous tissue from calcified tissue were improved.

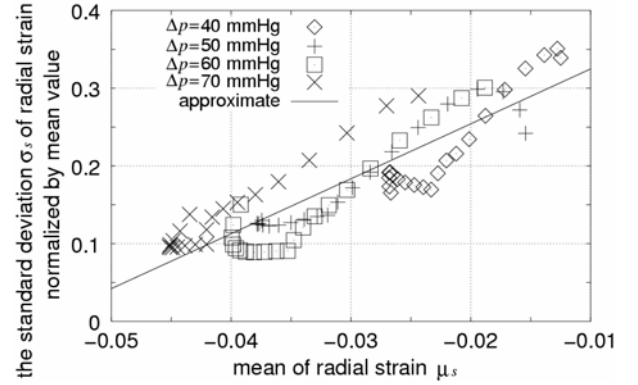


Fig. 13. Relationship between mean μ_s and standard deviation σ_s normalized by mean μ_s of the measured strains of the phantom.

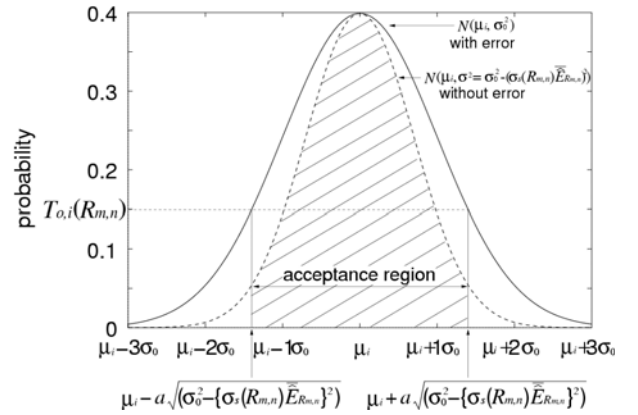


Fig. 14. Illustration of a method for determining threshold $T_{o,i}(R_{m,n})$ to likelihood function $L_i(m, n)$.

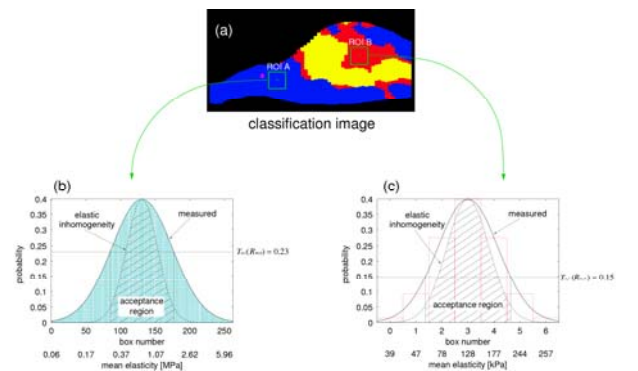


Fig. 15. Example of determination of threshold $T_{o,i}(R_{m,n})$ to likelihood function $L_i(m, n)$.

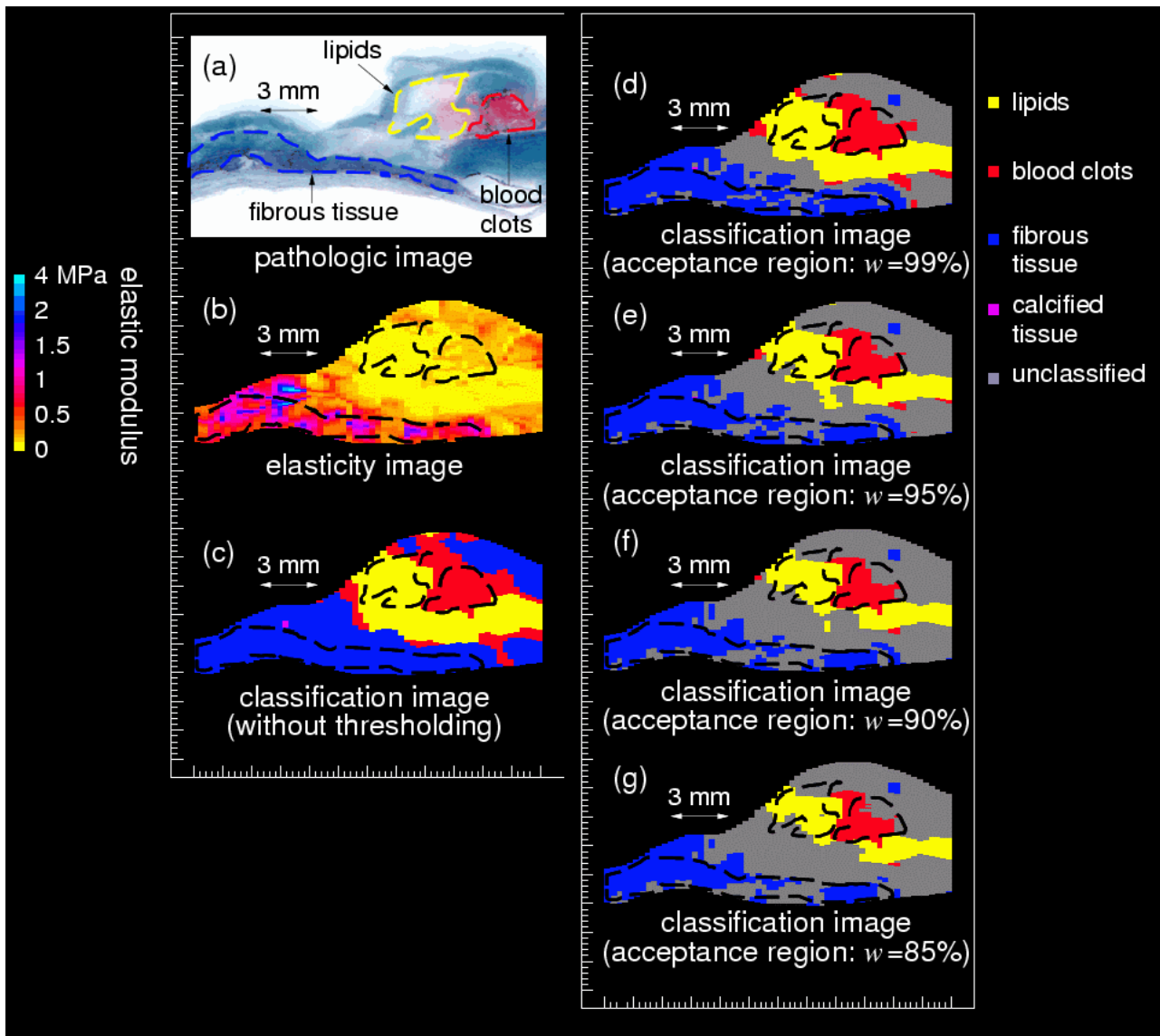


Fig. 16. Results of tissue classification for iliac artery (A). (a) Pathological image. (b) Elasticity image. Tissue classification images obtained with (c) no thresholding, (d) $T_{o,i}(R_{m,n})$ at $w=99\%$, (e) $T_{o,i}(R_{m,n})$ at $w=95\%$, (f) $T_{o,i}(R_{m,n})$ at $w=90\%$, and (g) $T_{o,i}(R_{m,n})$ at $w=85\%$.

References

- [1] Lee RT, Grodzinsky AJ, Frank EH, Kamm RD and Schoen FJ. Structure-dependent dynamic mechanical behavior of fibrous caps from human atherosclerotic plaques. *Circulation* **83**, 1764–1770, 1991.
- [2] Loree HM, Grodzinsky AJ, Park SY, Gibson LJ and Lee RT. Static circumferential tangential modulus of human atherosclerotic tissue. *J Biomech* **27**, 195–204, 1994.
- [3] Simons PCG, Algra A, Bots ML, Grobbee DE and van der Graaf Y. Common carotid intima-media thickness and arterial stiffness. *Circulation* **100**, 951–957, 1999.
- [4] Falk E, Shah PK and Fuster V. Coronary plaque disruption. *Circulation* **92**, 657–671, 1995.
- [5] Davies MJ. Stability and instability: Two faces of coronary atherosclerosis. *Circulation* **94**, 2013–2020, 1996.
- [6] Golledge J, Greenhalgh RM and Davies AH. The symptomatic carotid plaque. *Stroke* **31**, 774–781, 2000.
- [7] McConnell MV, Aikawa M, Maier SE, Ganz P, Libby P and Lee RT. MRI of rabbit atherosclerosis in response to dietary cholesterol lowering. *Arterioscler Thromb and Vasc Biol* **19**, 1956–1959, 1999.
- [8] Potkin BN, Bartorelli AL, Gessert JM, Neville RF, Almagor Y, Roberts WC and Leon MB. Coronary artery imaging with intravascular high-frequency ultrasound. *Circulation* **81**, 1575–1585, 1990.
- [9] Hoeks APG, Ruissen CJ, Hick P and Reneman RS. Transcutaneous detection of relative changes in artery diameter. *Ultrasound Med Biol* **11**, 51–59, 1985.
- [10] Hoeks APG, Di X, Brands PJ and Reneman RS. Comparison of the performance of the RF cross correlation and Doppler autocorrelation technique to

estimate the mean velocity of simulated ultrasound signals. *Ultrasound Med Biol* **19**, 727–740, 1993.

[11] Länne T, Stale H, Bengtsson H, Gustafsson D, Bergqvist D, Sonesson B, Lecerof H and Dahl P. Noninvasive measurement of diameter changes in the distal abdominal aorta in man. *Ultrasound Med Biol* **18**, 451–457, 1992.

[12] Brands PJ, Hoeks APG, Rutten MC and Reneman RS. A noninvasive method to estimate arterial impedance by means of assessment of local diameter change and the local centerline blood flow velocity using ultrasound. *Ultrasound Med Biol* **22**, 895–905, 1996.

[13] Meinders JM, Brands PJ, Willigers JM, Kornet L and Hoeks APG. Assessment of the spatial homogeneity of artery dimension parameters with high frame rate 2-D B-mode. *Ultrasound Med Biol* **27**, 785–794, 2001.

[14] Bergel DH. The static elastic properties of the arterial wall. *J Physiol* **156**, 445–457, 1961.

[15] Peterson LH, Jensen RE and Parnel J. Mechanical properties of arteries *in vivo*. *Circ Res* **8**, 622–639, 1960.

[16] Hayashi K, Handa H, Nagasawa S, Okamura A and Moritake K. Stiffness and elastic behavior of human intracranial and extracranial arteries. *J Biomech* **13**, 175–184, 1980.

[17] Kanai H, Sato M, Koiwa Y and Chubachi N. Transcutaneous measurement and spectrum analysis of heart wall vibrations. *IEEE Trans Ultrason Ferroelect Freq Contr* **43**, 791–810, 1996.

[18] Kanai H, Hasegawa H, Chubachi N, Koiwa Y and Tanaka M. Noninvasive evaluation of local myocardial thickening and its color-coded imaging. *IEEE Trans Ultrason Ferroelect Freq Contr* **44**, 752–768, 1997.

[19] Hasegawa H, Kanai H, Koiwa Y and Chubachi N. Noninvasive evaluation of Poisson's ratio of arterial wall using ultrasound. *Electron Lett* **33**, 340–342, 1997.

[20] Hasegawa H, Kanai H and Koiwa Y. Modified phased tracking method for measurement of change in thickness of arterial wall. *Jpn J Appl Phys* **41**, 3563–3571, 2002.

[21] Kanai H, Koiwa Y and Zhang J. Real-time measurements of local myocardium motion and arterial wall thickening. *IEEE Trans Ultrason Ferroelec Freq Contr* **46**, 1229–1241, 1999.

[22] Kanai H, Hasegawa H, Ichiki M, Tezuka F and Koiwa Y. Elasticity imaging of atheroma with transcutaneous ultrasound -preliminary study-. *Circulation* **107**, 3018–3021, 2003.

[23] Hasegawa H and Kanai H. Modification of the phased tracking method for reduction of artifacts in estimated artery wall deformation. *IEEE Trans Ultrason Ferroelect Freq Contr* **53**, 2050–2064, 2006.

[24] Jespersen SK, Wilhjelm JE and Sillesen H. Multi-angle compound imaging. *Ultrason Imag* **20**, 81–102, 1998.

[25] Hasegawa H, Kanai H, Hoshimiya N and Koiwa Y. Evaluating the regional elastic modulus of a cylindrical shell with nonuniform wall thickness. *J Med Ultrason* **31**, 81–90, 2004.

[26] Inagaki J, Hasegawa H, Kanai H, Ichiki M and Tezuka F. Construction of reference data for tissue characterization of arterial wall based on elasticity images. *Jpn J Appl Phys* **44**, 4593–4597, 2005.

[27] Inagaki J, Hasegawa H, Kanai H, Ichiki M and Tezuka F. Tissue classification of arterial wall based on elasticity image. *Jpn J Appl Phys* **45**, 4732–4735, 2006.

[28] Tsuzuki K, Hasegawa H, Kanai H, Ichiki M and Tezuka F. Optimal region-of-interest settings for tissue characterization based on ultrasonic elasticity imaging. *Ultrasound Med Biol* **34**, 573–585, 2008.

[29] Tsuzuki K, Hasegawa H, Kanai H, Ichiki M and Tezuka F. Threshold setting for likelihood function for elasticity-based tissue characterization of arterial wall by evaluating variance in measurement of radial strain. *Jpn J Appl Phys* **47**, 4180–4187, 2008.

[30] Timoshenko SP and Goodier JN. *Theory of Elasticity*, McGraw-Hill, Tokyo, 1970.

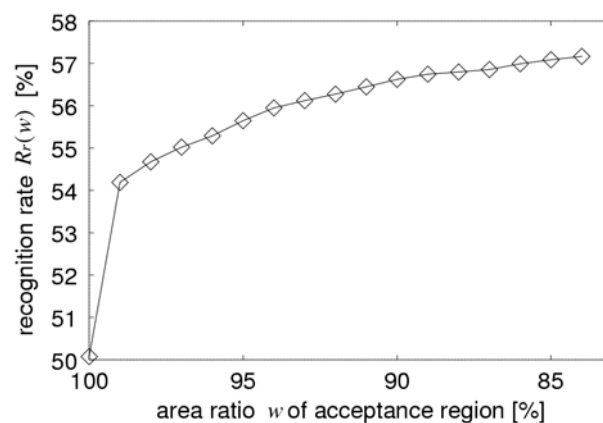


Fig. 17. Recognition rate $R_r(w)$ plotted as a function of acceptance region w .